J|A|C|S
A R T I C L E S

Neutral Complexes of First Row Transition Metals Bearing Unbound Thiocyanates and Their Assembly on Metallic Surfaces

Jacob W. Ciszek,[†] Zachary K. Keane,[‡] Long Cheng,[†] Michael P. Stewart,[†] Lam H. Yu,[‡] Douglas Natelson,*,[‡] and James M. Tour*,[†]

Contribution from the Department of Chemistry and Smalley Institute for Nanoscale Science and Technology, and Department of Physics and Astronomy, Rice University, 6100 Main Street, Houston, Texas 77005

Received August 24, 2005; E-mail: natelson@rice.edu; tour@rice.edu

Abstract: A series of transition metal coordination complexes designed to assemble on gold surfaces was synthesized, their electronic structure and transitions analyzed, and their magnetic properties studied. By taking advantage of recently developed thiocyanate assembly protocols, these molecules were then assembled onto a gold surface, without the need for an inert atmosphere, to give a loosely packed monolayer. The assembled molecules exhibit properties similar to that of the bulk molecules, indicating little change in molecular structure outside of chemisorption.

Introduction

Watershed events for the molecular electronics community were the measurements of single molecule conductance by several groups.[1–7] Following these demonstrations, scientists began to propose and measure electronic behavior attributed to single or small ensembles of molecules. Recent significant contributions to this field include papers on the Kondo effect[8–10] and inelastic electron tunneling spectroscopy (IETS)[11–14] in individual molecules. These papers explored quantum phenomena[15–18] in individual molecules that were part of

metal–molecule–metal junctions. These analyses supported the concept of molecular devices and also provided a bridge connecting traditional synthetic and analytical chemistry with molecular electronics.

We have extended this work by synthesizing a new series of metal-containing molecules. The purpose of the metal core is two-fold. First, one can discern which electronic effects in the junction are due to the metal atom core by varying the metal. Second, one can study the effect of different spin states on molecular conductance. Here we describe the efficient synthesis of these molecules and the simple techniques necessary for assembling them along with detailed characterization data of the assembled compounds on gold surfaces. From these data we can determine with high confidence the nature of the molecules after assembly.

The molecular system described here is of particular interest as it has been examined by both the theoretical and experimental branches of science. These compounds have been studied in electromigration-fabricated single molecule transistors (SMT) (Figure 1a). When examined in SMTs[13,19,20] these molecules have conductance features characteristic of the Kondo effect, a coherent many-body state comprising an unpaired spin on the molecule coupled by exchange to the conduction electrons of the leads.[13,20] Kondo temperatures in excess of 50 K were found, comparable to those in a purely metallic system.[20] In addition to the Kondo resonance some of these SMTs exhibit inelastic co-tunneling features that correspond energetically to vibrational excitations of the molecule, as determined by Raman and infrared spectroscopy.[13] This is a form of IETS of single

[†] Department of Chemistry and Smalley Institute for Nanoscale Science and Technology.

[‡] Department of Physics and Astronomy.

(1) Reed, M. A.; Zhou, C.; Muller, C. J.; Burgin, T. P.; Tour, J. M. *Science* **1997**, *278*, 252–254.

(2) Bumm, L. A.; Arnold, J. J.; Cygan, M. T.; Dunbar, T. D.; Burgin, T. P.; Jones, L, II; Allara, D. L.; Tour, J. M.; Weiss, P. S. *Science* **1996**, *271*, 1705–1707.

(3) Dorogi, M.; Gomez, J.; Osifchin, R.; Andres, R. P.; Reifenberger, R. *Phys. Rev. B: Condens. Matter* **1995**, *52*, 9071–9077.

(4) Andres, R. P.; Bein, T.; Dorogi, M.; Feng, S.; Henderson, J. I.; Kubiak, C. P.; Mahoney, W.; Osifchin, R. G.; Reifenberger, R. *Science* **1996**, *272*, 1323–1325.

(5) Joachim, C.; Gimzewski, J. K. *Europhys. Lett.* **1995**, *30*, 409–414.

(6) Joachim, C.; Gimzewski, J. K.; Schlittler, R. R.; Chavy, C. *Phys. Rev. Lett.* **1995**, *74*, 2102–2105.

(7) Fischer, C. M.; Burghard, M.; Roth, S.; Klitzing, K. v. *Appl. Phys. Lett.* **1995**, *66*, 3331–3333.

(8) Park, J.; Pasupathy, A. N.; Goldsmith, J. I.; Chang, C.; Yaish, Y.; Petta, J. R.; Rinkoski, M.; Sethna, J. P.; Abruna, H. D.; McEuen, P. L.; Ralph, D. C. *Nature* **2002**, *417*, 722–725.

(9) Liang, W.; Shores, M. P.; Bockrath, M.; Long, J. R.; Park, H. *Nature* **2002**, *417*, 725–729.

(10) Yu, L. H.; Natelson, D. *Nano Lett.* **2004**, *4*, 79–83.

(11) Kushmerick, J. G.; Lazorcik, J.; Patterson, C. H.; Shashidhar, R.; Seferos, D. S.; Bazan, G. C. *Nano Lett.* **2004**, *4*, 639–642.

(12) Wang, W.; Lee, T.; Kretzschmar, I.; Reed, M. A. *Nano Lett.* **2004**, *4*, 643–646.

(13) Yu, L. H.; Keane, Z. K.; Ciszek, J. W.; Cheng, L.; Stewart, M. P.; Tour, J. M.; Natelson, D. *Phys. Rev. Lett.* **2004**, *93*, 266802.

(14) Stipe, B. C.; Rezaei, M. A.; Ho, W. *Science* **1998**, *280*, 1732–1735.

(15) Kondo, J. *Prog. Theor. Phys.* **1964**, *32*, 37–49.

(16) Anderson, P. W. *Phys. Rev.* **1961**, *124*, 41–53.

(17) Jaklevic, R. C.; Lambe, J. *Phys. Rev. Lett.* **1966**, *17*, 1139–1140.

(18) Adkins, C. J.; Phillips, W. A. *J. Phys. C: Solid State Phys.* **1985**, *18*, 1313–1346.

(19) Natelson, D.; Yu, L. H.; Ciszek, J. W.; Keane, Z. K.; Tour, J. M. *Chem. Phys.* **2006**. In press

(20) Yu, L. H.; Keane, Z. K.; Ciszek, J. W.; Cheng, L.; Tour, J. M.; Baruah, T.; Pederson, M. R.; Natelson, D. *Phys. Rev. Lett.* **2005**, *95*, 256803.
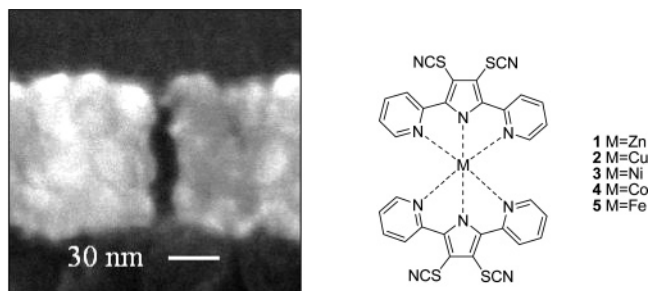
Figure 1. (a) SEM image of a junction used in the testing of the molecular devices.[13,19,22] Current transport likely occurs through the small area at the top portion of the junction where the gap distance is similar to the molecular dimensions. When current transport through a sufficiently small area, it is dominated by a single molecule. (b) Targeted molecular systems synthesized for this study.
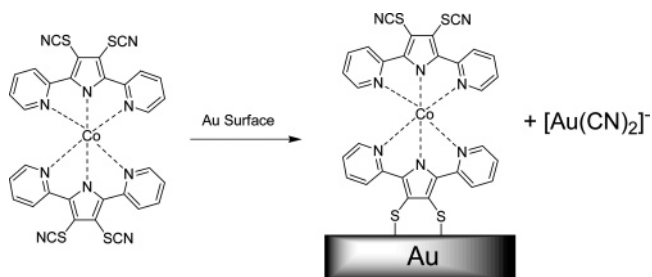
Figure 2. Schematic of the assembly on gold.

molecules, with transistor geometry allowing in situ tuning of the electronic states via a gate electrode. The molecules have also been modeled using the Green function approach and have been predicted to exhibit good hole conduction.[21]

The compounds **1−5** (Figure 1b) were synthesized with several parameters in mind. First, these molecules were designed to have a simple assembly protocol on metal where they are stable to air yet active toward a metal surface without the use of exogenous reagents. We have taken advantage of our recently published thiocyanate assembly procedure, in which the thiocyanate is converted to a thiolate via the gold surface, and the cyanide leaves as $[Au(CN)_2]^-$.[22,23] Thus, the metal complexes spontaneously assemble on a clean gold surface (Figure 2). Use of the thiocyanates eliminates the need for the oxidatively unstable aromatic free thiols or their thioacetate precursors.[24−26]

When designing these molecules we wanted to avoid parasitic charges that may interfere with the solid-state electrical studies of the molecules as SMTs. Thus the system was designed to be overall neutral (no counterions). To facilitate molecular conduction, the molecules were designed to be small and contain a continuous π-electron system that is interrupted only by the core in order to force electrons through the metal atom. Finally, the molecules were designed such that all coordination sites on the metal atom were bound by multi-dentate ligands. This is important since it minimizes ligand dissociation and retards effects that may influence electrical studies, such as decom-

plexation, ligand exchange, or complexation of trace species such as water. Occupation of all coordination sites is also essential as these molecules are designed to contain a moiety (sulfur) for binding to metal surfaces in the presence of a metal core. If there were free coordination sites they could lead to complexation of the sulfur or cyanide with the metal core. The two tridentate ligands therefore protect the molecule from self-decomposition.

Experimental Section

Materials. The syntheses of all compounds can be found in the Supporting Information, along with characterization including: [1]H, ^{13}C, IR (powder and surface), magnetic susceptibility, EPR, CV, UV−vis, DSC, TGA, MS, elemental analysis, and XPS (powder and surface). Ethanol (100%) was obtained from Pharmco. THF was freshly distilled (sodium, benzophenone) prior to use. Dichloromethane was distilled from calcium hydride. All metals were of 99.99% or greater purity. Silicon ⟨100⟩ wafers (p doped, test grade) were obtained from Silicon Quest International. Gold coated mica was purchased from Molecular Imaging.

EPR. All EPR samples were prepared by dissolving the metal complexes in freshly distilled THF (ca. 10 μM, **2**; 100 μM, **4**). Solutions were passed through a 0.2 μm nylon filter and then quickly frozen. Spectra were taken in a Varian E6 X-band spectrometer with an Air Products helium cryogenic system.

Magnetic Susceptibility. Magnetic susceptibility measurements were taken in a Superconducting Quantum Interference Device (SQUID). Analysis was carried out at temperatures from 300 to 1.7 K using a Quantum Design MPMS-5S magnetometer.

Cyclic Voltammetry. Electrochemical characterization was carried out with a Bioanalytical Systems (BAS CV-50W) analyzer. The reference was a Ag|AgNO₃ electrode. The counter electrode was a clean Pt wire. Redox potentials were determined at the specified scan rates. The solutions studied were 1 mM with 0.1 M tetrabutylammonium tetrafluoroborate as the supporting electrolyte in THF under inert atmosphere.

UV−Visible Absorbance. UV−vis spectra were acquired on a Shimadzu UV-3101PC containing both a deuterium and halogen light source. All spectra were collected in freshly distilled dichloromethane.

Preparation of Evaporated Metal Substrates. All metal substrates were prepared by thermal evaporation with a base pressure of ∼1 × 10⁻⁶ Torr on test grade ⟨100⟩ silicon wafers with a typical evaporation rate of 1 Å/s. A chromium adhesion layer (5 nm) was applied to all substrates prior to deposition of 150 nm of the metal. All substrates were used within 20 min after removal from the vacuum chamber.

Assembly Procedure. Molecules were assembled onto freshly prepared substrates in freshly distilled dichloromethane or THF at a concentration of 0.5−1.0 mM. Assemblies typically proceeded for 24 h in the dark, after which they were vigorously rinsed with the same solvent used for assembly and dried under a stream of nitrogen.

Ellipsometric Measurements. Measurements of surface optical constants and molecular layer thicknesses were taken with a single wavelength (632.8 nm laser) LSE Stokes Ellipsometer (Gaertner Scientific). The surface thickness was modeled as a single absorbing layer atop an infinitely thick substrate (fixed n_s). The observed error in repeated measurements of the same spot was typically 0.2 nm or less. The index of refraction was set at 1.55.

Infrared Reflection Spectroscopy Measurements. A Nicolet Nexus 670 spectrometer with KBr beam splitter and MCT/A detector was used in conjunction with a SMART/SAGA grazing angle accessory, using a 16 mm diameter sampling area with p-polarized light fixed at an 80° angle of incidence.

X-ray Photoelectron Spectroscopy (XPS) Measurements. A PHI Quantera SXM XPS/ESCA system at 5 × 10⁻⁹ Torr was used to take photoelectron spectra. A monochromatic Al X-ray source at 100 W

(21) Yan, L.; Seminario, J. M. *J. Phys. Chem. A* **2005**, *109*, 6628−6633.
(22) Ciszek, J. W.; Stewart, M. P.; Tour, J. M. *J. Am. Chem. Soc.* **2004**, *126*, 13172−13173.
(23) Ciszek, J. W.; Tour, J. M. *Chem. Mater.* **2005**, *17*, 5684−5690.
(24) Bain, C. D.; Troughton, E. B.; Tao, Y.-T.; Evall, J.; Whitesides, G. M.; Nuzzo, R. G. *J. Am. Chem. Soc.* **1989**, *111*, 321−335.
(25) Tour, J. M.; Jones, L., II; Pearson, D. L.; Lamba, J. J. S.; Burgin, T. P.; Whitesides, G. M.; Allara, D. L.; Parikh, A. N.; Atre, S. V. *J. Am. Chem. Soc.* **1995**, *117*, 9529−9534.
(26) Stapleton, J. J.; Harder, P.; Daniel, T. A.; Reinard, M. D.; Yao, Y.; Price, D. W.; Tour, J. M.; Allara, D. L. *Langmuir* **2003**, *19*, 8245−8255.

Scheme 1. Synthesis of the Simple Ligand **8**

**Scheme 2.** Formation of the Metal Complex Test Cases
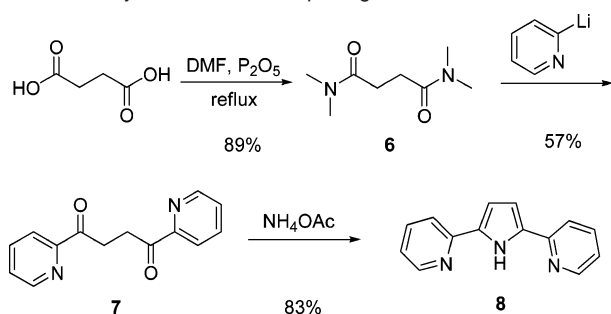
was used with an analytical spot size of 0.15 mm × 1.4 mm and a 45° takeoff angle, with a pass energy of 26.00 eV. High-resolution spectra of the S 2p region used a 45° takeoff angle and 13.00 eV pass energy. Unless noted, surface samples were referenced against the internal Au $4f_{7/2}$ line at 84.0 eV. Crystalline powder samples were referenced externally to an Au 4f peak at 84.00 eV and internally to a C 1s binding energy of 284.50 eV (NIST XPS database). Atomic concentration values were calculated with PHI Multipak software using factory-calibrated values for the sensitivity factors of the respective elements.

Computational Procedures. Theoretical calculations were performed by using the Gaussian 98[27] program. The calculations were performed on the crystallographic structures. The energy calculation was performed using the reduced Hartree–Fock method with the SDD basis set.[28,29] The output was visualized with gopenmol.[30,31]

Synthesis

The basic design was to have a metal(II) atom surrounded by two anionic ligands (Figure 1b). Hence, a ligand such as **8** was a natural choice (Scheme 1). Although this ligand had been synthesized previously[32] and even complexed on one occasion,[33] we found all previous methods to be impractical for large-scale synthesis. Thus, our preferred route to **8** begins with succinic acid that was converted to the bis-acetimide **6** in 89% yield using a slightly modified version of Schindlbauer's method.[34] This was then converted to the bis-pyridal system **7** with a modification of conditions outlined by Owsley.[35] Cyclization using ammonium acetate[32] gave **8**. This ligand was deprotonated and reacted with $ZnCl_2$ and $CoCl_2$ to produce **9** and **10**, respectively, as test cases for the complexation (Scheme 2).

With complexation successfully demonstrated, the possible methods for attachment of the molecules to metal surfaces were examined. The 4-positions of the pyridine rings and 3,4-positions of the pyrrole ring both suggest themselves as viable sites for functional groups that will attach to the surface.[36] We focused on substitution at the 3- and 4-positions of the pyrrole ring.
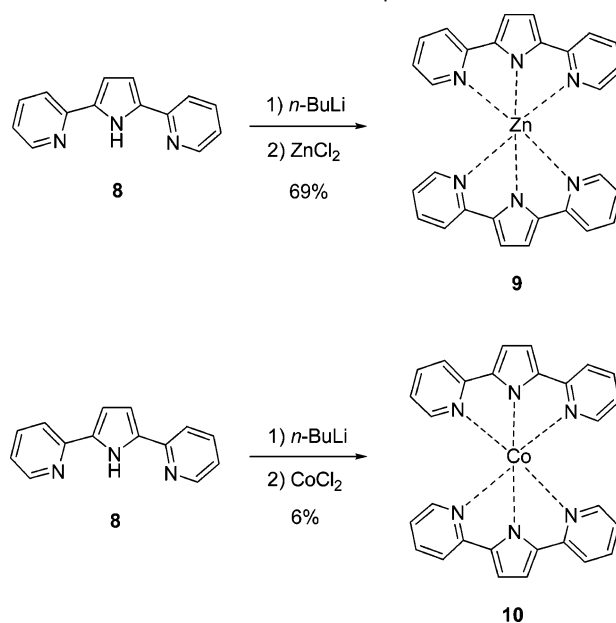
Scheme 3. Synthesis of Thiocyanate-Containing Ligands[a]
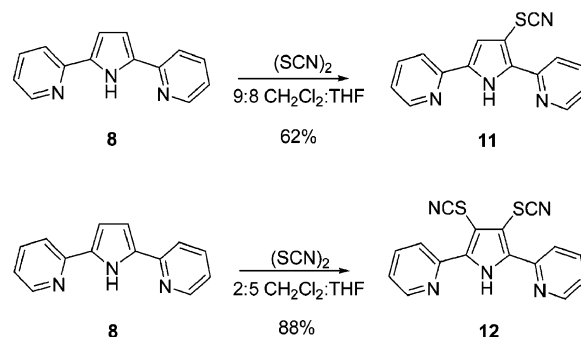
[a] Solvent conditions determine whether the mono- or dithiocyanate species is preferentially formed.

Thiocyanates were chosen as surface-binding precursors since they offer many of the advantages of the thiol on gold chemistry (such as rearrangement on a surface,[37] an important factor for such a bulky molecule) without the oxidative instability found in the free thiols.[25] This system has the advantage of not requiring any extraneous materials or inert conditions, and gives the same structure on gold as an assembly from a free thiol (Figure 2).

Accordingly, the mono- and dithiocyanate functionalized ligands **11** and **12** were synthesized by treating the bare ligand with thiocyanogen $((SCN)_2$, generated from $Pb(SCN)_2$ and Br_2). In a mixture of 9:8 CH_2Cl_2/THF the monothiocyanate **11** was formed preferentially, whereas in a more polar mixture (2:5 CH_2-Cl_2/THF) the major product was the dithiocyanate **12** (Scheme 3). For complexation, **12** was deprotonated with NaH and then combined with the metal halide to give the final metal complexes **1**−**5** in varying yield. The iron compound **5** was meta-stable, allowing only partial characterization (Scheme 4).

Metal Complex Characteristics

The metal complexes are intended to be studied in a variety of molecular electronic testbeds.[38] The results of the tests will

(27) Frisch, M. J.; et al. *Gaussian 98*, Revision A.11; Gaussian Inc.: Pittsburgh, PA, 2001.
(28) Dunning, T. H. J.; Hay, P. J. *Modern Theoretical Chemistry*; Plenum Press: New York, 1977; Vol. 3.
(29) Igel-Mann, G.; Stoll, H.; Preuss, H. *Mol. Phys.* **1988**, *65*, 1321−1328.
(30) Bergman, D. L.; Laaksonen, L.; Laaksonen, A. *J. Mol. Graphics Model.* **1997**, *15*, (301−306).
(31) Laaksonen, L. *J. Mol. Graphics* **1992**, *10*, 33−34.
(32) Jones, R. A.; Karatza, M.; Voro, T. N.; Civcir, P. U.; Franck, A.; Ozturk, O.; Seaman, J. P.; Whitmore, A. P.; Williamson, D. J. *Tetrahedron* **1996**, *52*, 8707−8724.
(33) Hein, B.; Beierlein, U. *Pharma. Zentralhalle* **1957**, *96*, 401−421.
(34) Schindlbauer, H. *Monatsh. Chem.* **1968**, *99*, 1799−1807.
(35) Owsley, D. C.; Nelke, J. M.; Bloomfield, J. J. *J. Org. Chem.* **1973**, *38*, 901−903.
(36) The design is such that there is a continuous conducting π system throughout the molecule except were the electrons are forced to travel through the metal atom. The alligator clips must be in a position such that each metal lead in a SMT attaches to only one ligand, and thus, electrons travel from lead to lead through the metal center as opposed to from end to end of one ligand.
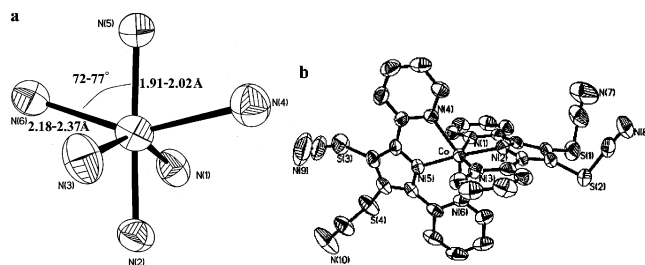
(37) Ulman, A. *Chem. Rev.* **1996**, *96*, 1533−1554.

Scheme 4. Complexation of the Free Ligand **12** with the Metal Halide
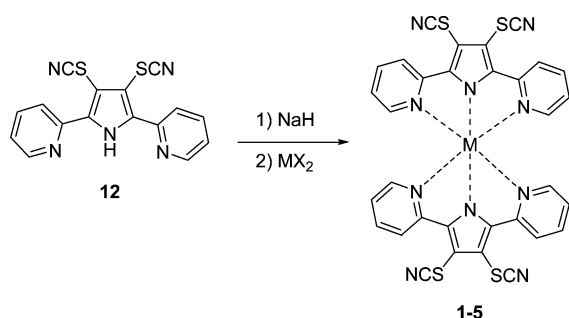
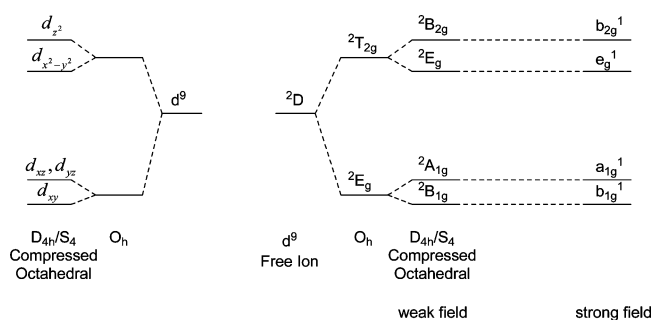| Metal salt	Product	Yield (%)
$ZnCl_2$	**1**	91
$CuBr_2$	**2**	72
$NiBr_2$	**3**	43
$CoCl_2$	**4**	72
$FeCl_2$	**5**	15

Table 1. Bond Distance and Angle Deviations from O_h Symmetry

metal	R_S (Å)	R_L (Å)	av N–M–N angle (deg)
Zn (**1**)	1.96	2.32	74
Cu (**2**)	1.89	2.26	75
Ni (**3**)	1.96	2.23	76
Co (**4**)	1.97	2.24	74
Fe (**5**)	2.03	2.27	74

Figure 3. Structural details of compounds **1**–**5**. (a) The relevant bond distances and angles of **1**–**5**. (b) ORTEP of **4** from X-ray crystallography.

be correlated with spectroscopic data to show these individual molecular effects in electronic devices.[11–13,20] The physical characterization data discussed here will focus primarily on molecular properties that will contribute to the discussion of the SMT data. An expansive version of the characterization can be found in the Supporting Information.

Structure and Crystal Field Splitting. The target compounds **1**–**5** share the same geometry. The complexes can be called compressed octahedra, an uncommon species[39,40] (Table 1, Figure 3). On average the M–N$_{pyrrole}$ bond distances (along the Z axis) are 0.2–0.3 Å shorter than the M–N$_{pyridine}$ bond distances. For a compressed octahedral species, it is common to predict the crystal field splitting based from an O_h symmetry with the appropriate distortions noted (taking into account only the immediate environment of the metal[41]). The extent of

(38) Tour, J. M. *Molecular Electronics: Commercial Insights, Chemistry, Devices, Architecture and Programming*; World Scientific: River Edge, New Jersey, 2003.
(39) Halcrow, M. A. *J. Chem. Soc., Dalton Trans.* **2003**, 4375–4384.
(40) Murphy, A.; Mullane, J.; Hathaway, B. *Inorg. Nucl. Chem. Lett.* **1980**, *16*, 129–134.
(41) Figgis, B. N. *Introduction to Ligand Fields*; John Wiley & Sons: New York, 1966.

Figure 4. Crystal field splitting and correlation diagram for **2**.

tetragonal distortion (T, where $T = R_S/R_L$)[42] is not unusually large (0.84–0.89) and supports treatment of the complexes as compressed octahedra. Asymmetry that is not consistent with compressed octahedra is observed in the bond angles. The rigidity of the ligand results in N–M–N bond angles which deviate from 90° (an average of 74–76°). This is only slightly larger than the typical Jahn–Teller distortion commonly seen for coordination compounds including Cu(dien)$_2$(NO$_3$)$_2$ (79–80°), one of the few well-studied compressed octahedral compounds,[42–44] which will serve as the basis for comparison in our work. Though the true symmetry of the molecule is S_4, the symmetry elements are similar to D_{4h}, and thus much of the literature can be used interchangeably.

The crystal field splitting expected from S_4/D_{4h} symmetry is illustrated in Figure 4. The splitting (and the associated transitions in the UV–vis spectrum) is somewhat ambiguous. The d$_{z^2}$ orbital is the highest in energy (by EPR spectroscopy vide infra), lying above the d$_{x^2−y^2}$ orbital. It is generally accepted[39,44,45] that the d$_{xz}$ and d$_{yz}$ orbitals lie at a slightly higher energy than the d$_{xy}$ orbital, although there has been some question as to the latter assignment.[43] Since we have no experimental evidence to suggest otherwise, we use the standard ordering (Figure 4).

UV–Vis 43000-6250 cm^{-1} (230–1600 nm). Building on the preceding discussion of the relative energies of the d orbitals, we examined the various d electron transitions in complexes **2**–**5**. The assignments of the absorption features of **2** are relatively straightforward (Table 2) and are consistent with the expected transitions. Assignments for the other metals are problematic. For nickel(II) (d^8), the correlation diagram gets more complex (Figure 5a) with 11 different terms for O_h symmetry and 19 when S_4 symmetry is taken into account. Cobalt(II) (d^7) has seven free ion terms, and 19 in the simple case of O_h symmetry. Thus, the cobalt spectrum generally contains many broad indistinguishable features that can only be resolved at very low temperatures.[46,47]

Nickel has been studied in greater detail, although low temperature is again necessary for full detailed studies of this system. For nickel we would expect three main sets of transitions (O_h symmetry) corresponding to the spin allowed transitions ($^3A_{2g}$ to $^3T_{2g}$, $^3T_{1g}$, and $^3T_{1g}$ (P)) (Figure 5). Each of these

(42) Procter, I. M.; Hathaway, B. J.; Nicholls, P. *J. Chem. Soc. A* **1968**, 1678–1684.
(43) Hathaway, B. J.; Bew, M. J.; Billing, D. E. *J. Chem. Soc. A* **1970**, 1090–1095.
(44) Stephens, F. S. *J. Chem. Soc. A.* **1969**, 883–890.
(45) Pilbrow, J. R. *Transition Ion Electron Paramagnetic Resonance*; Clarendon Press: Oxford, 1990.
(46) Ferguson, J.; Wood, D. L.; Knox, K. *J. Chem. Phys.* **1963**, *39*, 881–889.
(47) Lever, A. B. P.; Walker, I. M.; McCarthy, P. J. *Inorg. Chim. Acta* **1980**, *39*, 81–90.

Table 2. Visible Transitions Observed in the Transition Metal Complexes

	absorption features[a]								
compound	λ, cm^{-1} (nm)	ϵ	transition	λ, cm^{-1} (nm)	ϵ	transition	λ, cm^{-1} (nm)	ϵ	transition
2 (Cu)	14290 (700)	28	$^2B_{1g} \rightarrow {}^2B_{2g}$ [b]	12990 (770)	46	$^2B_{1g} \rightarrow {}^2E_g$ [b]	8670 (1154)	189	$^2B_{1g} \rightarrow {}^2A_{1g}$
3 (Ni)	–	–	–	16420 (609)	17	"O_h T$_{1g}$" $^3B_{1g} \rightarrow {}^3E_g$ + $^3B_{1g} \rightarrow {}^3A_{2g}$	10550 (948) 9550 (1047)	31 31	$^3B_{1g} \rightarrow {}^3B_{2g}$ $^3B_{1g} \rightarrow {}^3E_g$ ($^3T_{2g}$, O_h)
4 (Co)[c]	15530 (644)	25	–	–	–	–	10830 (923)	19	–

[a] The spectra that are not shown are included in the Supporting Information. *[b]* See previous section for discussion on these particular transitions. *[c]* Features are very broad and possibly encompass multiple transitions.
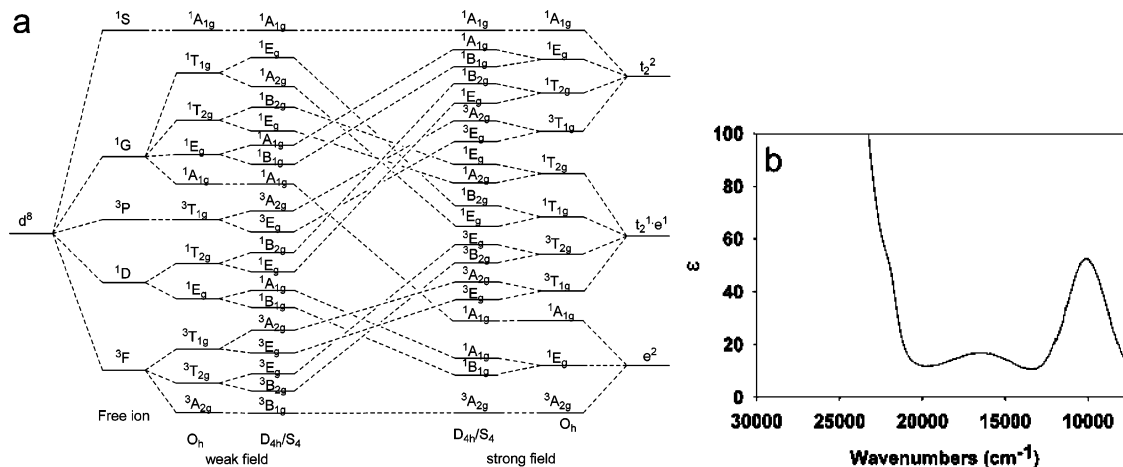
Figure 5. (a) Correlation diagram for octahedral and compressed octahedral splitting of the d^8 configuration. Energy is not to scale. For more details on calculating energy transitions of nickel(II) in D_{4h} fields see references 49−51. (b) Visible spectrum of **3**.

transitions will be split into two bands when the S_4 symmetry is taken into consideration. The transitions to $^3B_{2g}$ and ^3E_g ($^3T_{2g}$ in O_h) are expected to appear between 7500 and 12500 cm^{-1}.[47] Though the splitting between the two transitions is small ($\sim$1000 cm^{-1}) the spectrum can be deconvolved to show the $^3B_{2g}$ transition at 9550 cm^{-1} and the ^3E_g peak at 10550 cm^{-1} (Figure 5b). The two absorbances stemming from the $^3T_{1g}$ (O_h) state ($^3B_{1g} \rightarrow {}^3E_g$, $^3A_{2g}$) contain excessive overlap from other terms as well as charge transfer and $\pi \rightarrow \pi^*$ transitions and hence cannot be deconvolved. Thus, the peak at 16420 cm^{-1} is assigned to the combination of those two signals. The remaining spin-allowed and -forbidden transitions are obscured by the other larger signals. For cobalt, six low-energy spin-allowed transitions are expected. However, none of these are sufficiently resolved in order to make definite assignments.

Although the conjugated system is advantageous for transferring electrons throughout the molecule, the $\pi \rightarrow \pi^*$ transitions of the conjugated system makes assignment of the charge-transfer signals problematic. The ligand $\pi \rightarrow \pi^*$ and charge-transfer transitions are summarized in Figure 6 and Table 3.

EPR. The EPR spectrum of the copper compound allows for some confirmation of the predicted crystal field splitting. The measured **g** tensor can be predicted by the equation[51]

$$g_{\alpha\beta} = g_e\delta_{\alpha\beta} + 2\lambda \sum_{n'} \frac{\langle n|L_\alpha|n'\rangle\langle n|L_\beta|n'\rangle}{E_n - E_{n'}}$$

where n is the orbital containing the unpaired spin, n' is the
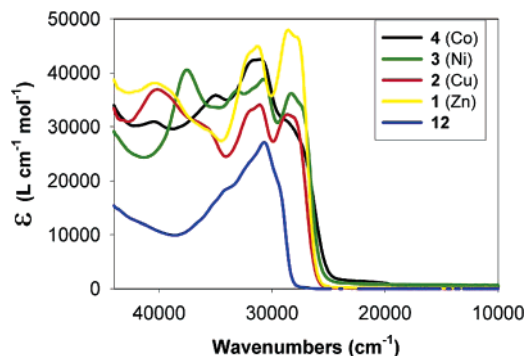
**Figure 6.** Charge transfer and $\pi \rightarrow \pi^*$ transitions in complexes **1**−**4**.

Table 3. UV Absorption Band for Compounds **1**−**4**

cmpd	transitions cm^{-1} (nm)			
12	–	–	30680 (326)	–
1 (Zn)	40490 (247)	–	31250 (320)	28570 (350)
2 (Cu)	40160 (249)	–	31150 (321)	28650 (349)
3 (Ni)	37590 (266)	33110 (302)	30770 (325)	28330 (353)
4 (Co)	40490 (247)	34970 (286)	30160 (322)	–

coupled orbital, L is the orbital angular momentum operator, g_e is the g-factor for a free electron, λ is the spin−orbit coupling constant and E represents the respective energy terms. If the unpaired electron lies in the d$_{z^2}$ orbital, the equation gives $g_{xx} = g_{yy} = g_e + 6\lambda/(E_{z^2} - E_{xz,yz})$ and $g_{zz} = g_e$. Hence, an experimental value of g_{zz} near that of a free electron (2.0023) and a larger $g_{xx,yy}$ is evidence for the predicted crystal field
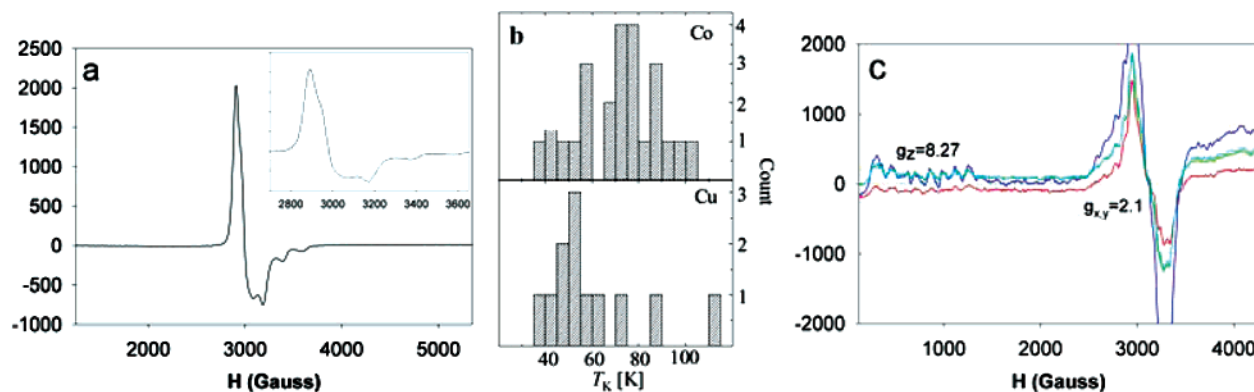
Figure 7. Magnetic properties of complexes **2** and **4**. (a) EPR spectrum of the copper complex **2**. Inlaid image is an enlarged portion of the spectrum. (b) A histogram of the Kondo temperatures measured for the cobalt complex **4** and the copper complex **2**.[20] (c) EPR spectrum of the cobalt complex **4** at various receiver gains.
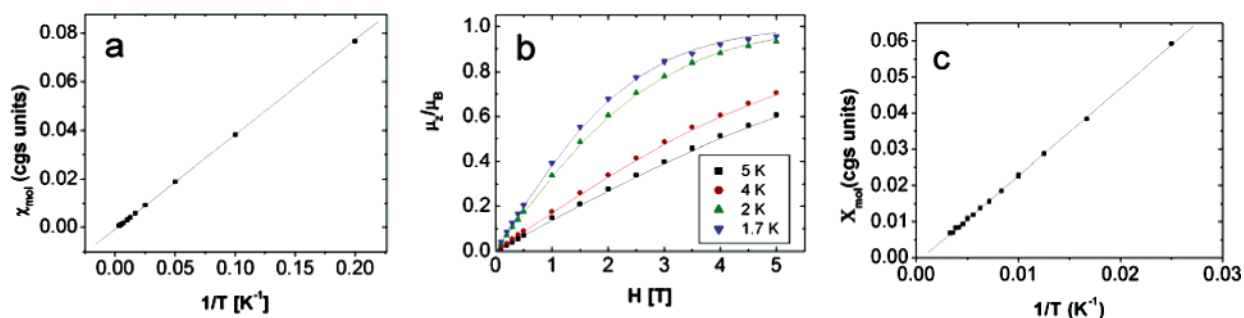
Figure 8. Magnetization data for **2** and **3**. (a) SQUID low-field data for copper compound **2**. (b) High-field data for compound **2**. (c) SQUID low-field data for nickel compound **3**.

splitting.[52] The respective measured values for $g_{\parallel}$ (g_{zz}) and $g_{\perp}$ (g_{xx}, g_{yy}) are 2.020 and ~2.22 (the small amount of uncertainty in the latter being due to hyperfine splitting appearing near the inflection point) (Figure 7a). This confirms the unpaired electron lies in the d_{z^2} orbital. The hyperfine splitting constant A is 200 G in the z direction. The hyperfine splitting constant is smaller than the line width for $g_{xx,yy}$.

By combining these results with the observed UV transitions, one can calculate λ' the observed spin−orbit coupling constant.[53,54] The ratio of λ'/λ provides a measure of the extent of covalency, or an indication as to the delocalization of the spin onto the ligand.[51,55] With d_{xy} as the lowest lying d orbital ($d_{xy} \rightarrow d_{z^2} = 700$ nm, see previous section), λ'/λ is equal to 0.57. This is quite low when compared to other simple copper(II) complexes.[56] It also provides experimental evidence that this compound contains a large amount of spin delocalization onto the ligands and has very good transport through the metal center.

Such experimental evidence is welcome as we have previously shown unusually high Kondo temperatures in SMTs (Figure 7b).[20] Kondo transport[15,16] (which can simplistically be thought of as electron transfer through unpaired spins) has a characteristic temperature that is exponentially sensitive to the

coupling between the transition metal and the conduction electrons of the electrodes (through the ligands) onto which the molecule is assembled. The measured Kondo temperatures are comparable to those observed in scanning tunneling microscopy measurements of transition metals directly bonded to gold surfaces. This large extent of delocalization provides an experimental explanation for such a high source-spin-drain coupling.

For the cobalt species (Figure 7c) we observe large magnetic anisotropy consistent with that seen in the literature for cobalt(II) where $S = ^3/_2$.[57] The large g factor (4.3) becomes anisotropic when the octahedral symmetry is distorted by trigonal[58] or tetragonal distortion.[59] This results in additional terms along the diagonal of the energy matrix which supplement spin−orbit coupling. Further discussion of this phenomenon can be found elsewhere.[45,57,60] In our system $g_{\perp}$ was observed to be 2.1 with $g_{\parallel}$ equal to 8.27. This large anisotropy along the z axis has also been observed in terpyridine complexes.[61] For **4** the hyperfine splitting constant A is 135 G in the z direction.

Magnetic Susceptibility. The magnetic susceptibilities of compounds **1**−**5** were examined by SQUID. Analysis of complexes **1**−**3** was straightforward. As expected, the zinc(II) complex **1** has no unpaired spins and is diamagnetic with a susceptibility of -4.68×10^{-4} emu/mol. The copper(II) complex **2** with a 3d[9] configuration behaves like a well-defined

(48) Schreiner, A. F.; Hamm, D. J. *Inorg. Chem.* **1973**, *12*, 2037−2048.
(49) Maki, G. *J. Chem. Phys.* **1958**, *28*, 651−662.
(50) Rowley, D. A.; Drago, R. S. *Inorg. Chem.* **1967**, *6*, 1092−1096.
(51) Atherton, N. M. *Principles of Electron Spin Resonance*; Horwood, PTR Prentice Hall: New York, 1993.
(52) Palmer, G. *Biochem. Soc. Trans.* **1985**, *13*, 548−560.
(53) Dunn, T. M. *J. Chem. Soc.* **1959**, 623−627.
(54) Owen, J. *Proc. R. Soc. London, Ser A.* **1955**, *227*, 183−200.
(55) Cotton, F. A.; Goodgame, D. M. L.; Goodgame, M. *J. Am. Chem. Soc.* **1961**, *83*, 4690−4699.
(56) Hathaway, B. J.; Billing, D. E.; Nicholls, P.; Procter, I. M. *J. Chem. Soc. A* **1969**, 319−325.

(57) Abragam, A.; Pryce, M. H. L. *Proc. R. Soc. London, Ser A.* **1951**, *206*, 173−191.
(58) Jesson, J. P. *J. Chem. Phys.* **1966**, *45*, 1049−1056.
(59) Bleaney, B.; Ingram, D. J. E. *Proc. R. Soc. London, A.* **1951**, *208*, 143−158.
(60) Abragam, A.; Bleaney, B. *Electron Paramagnetic Resonance of Transition Ions*; Clarendon Press: Oxford, 1970.
(61) Kremer, S.; Henke, W.; Reinen, D. *Inorg. Chem.* **1982**, *21*, 3013−3022.
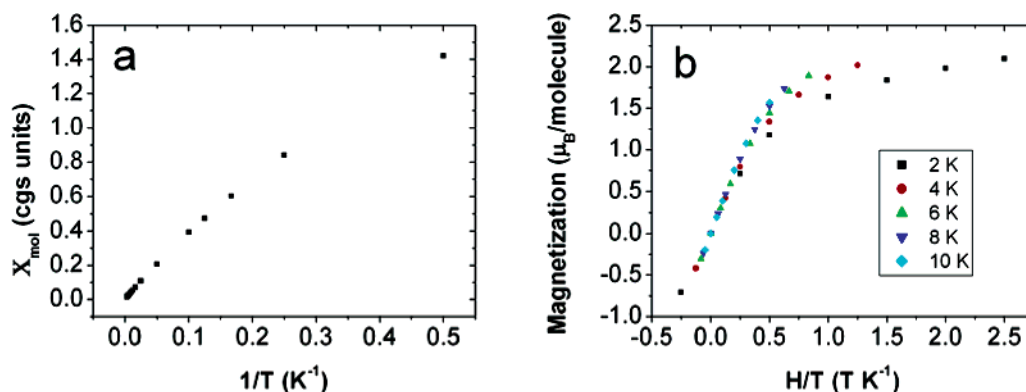
Figure 9. Magnetization data of for the iron complex **5**. (a) SQUID low-field data for **5**. (b) SQUID high-field data for **5**.

spin $^1/_2$ paramagnetic compound (Figure 8a,b). Low-field data gives a magnetic susceptibility of 1.76 μ_B, similar to the 1.73 μ_B expected for a spin $^1/_2$ compound with no orbital contributions. The high field data can be fit with a Brillouin function with $j = 0.5$ and $g = 2.02$. The nickel(II) species **3** is similarly straightforward at high temperatures with an effective magnetic moment of 4.3 μ_B.

The behavior of the cobalt(II) complex **4** was much more complex. We discovered from measurements on powders that this material's susceptibility is highly anisotropic; as a result we were forced to collect data from a particularly large single crystal (2.6 mg). The single crystal data indicates that the cobalt complex is strongly paramagnetic along one axis and weakly paramagnetic along the other two. According to low-field dc susceptibility measurements, the weakly paramagnetic axes have an effective magnetic moment of 2.6 μ_B, and the strongly paramagnetic axis gives an effective magnetic moment of 9.2 μ_B. The crystallographic axes are coincident with the molecular axes.

The magnetization data on the iron(II) complex **5** also yielded interesting information. While the data above ~6 K is highly suggestive of a system with four unpaired spins (with an effective magnetic moment of 5.9 μ_B), it is clear that the magnetization data plotted vs H/T below 6 K fall on different curves (Figure 9). This suggests that zero field splitting plays a significant role in the magnetic properties of the iron complex.[62,63] Alternatively, it is possible that the low-temperature data hint at the onset of a transition to a low-spin state.[64,65]

CV. From cyclic voltammetry we can see that all molecules are overall neutral with a metal(II) center (Table 4, Figure 10). As the potential is increased, nickel(II) **3**, cobalt(II) **4**, and iron(II) **5** complexes undergo a reversible oxidation to nickel-(III), cobalt(III), and iron(III), respectively. This reversible oxidation and reduction occurs at 0.87 and 0.77 V (vs Ag|AgNO$_3$, 20 mV/s) for nickel, −0.01 and 0.14 V for cobalt (20 mV/s), and 0.39 to 0.20 for iron (at 600 mV/s). It is worth noting that there is an extra feature at −0.69 V for iron. None of the other compounds (**1**−**4**) demonstrated this feature. When we further investigated this phenomenon we saw that it was not present when scanning from −0.1 to −1.0 V but was present when the scan was cycled from −1.0 to 0.75 V and

Table 4. Reversible Reductions/Oxidation[a] of the Metal Centers

cmpd	metal reduction	potential (V)	metal oxidation	potential (V)
2	$Cu^{II} \rightarrow Cu^{I}$	−0.80	$Cu^{I} \rightarrow Cu^{II}$	−0.66
3	$Ni^{III} \rightarrow Ni^{II}$	0.77	$Ni^{II} \rightarrow Ni^{III}$	0.87
4	$Co^{III} \rightarrow Co^{II}$	−0.012	$Co^{II} \rightarrow Co^{III}$	0.14
10	$Co^{III} \rightarrow Co^{II}$	−0.42	$Co^{II} \rightarrow Co^{III}$	−0.30
5	$Fe^{III} \rightarrow Fe^{II}$	0.20	$Fe^{II} \rightarrow Fe^{III}$	0.39

[a] The oxidations/reductions were performed on the metal complexes **1**−**5**, **10** (1 mM) in THF with 0.1 M TBABF$_4$ as the supporting electrolyte. The scan rate for all of the redox potentials was 20 mV/s with the exception of **5** which was at 600 mV/s. The potential is vs Ag/Ag$^+$.

then back to −1.0 V(Figure 11a). We surmise that this phenomenon is responsible for the reduction current peak (I_{pc}) always being smaller than the oxidation current peak (I_{pa}). Because the ratio of these two peaks approaches unity as the scan rate is increased (Figure 11b), it is natural to suggest that this is a rearrangement phenomenon (be it ligand association or dissociation), which is consistent with the lack of stability for **5** as mentioned earlier.

It was unsurprising that the redox potentials of the complexes **3**−**5** occur at a potential that is negative with respect to that of the analogous 2,6-bis(2-pyridyl)pyridine (terpy) complexes ($E_{1/2}$ for the II → III oxidation was 1.65 V for nickel, 0.31 V for cobalt, and 1.13 V for iron, vs SSCE).[66,67] The terpy ligand is neutral while our complexes use **12** as an anionic ligand, and thus a substantial difference in redox potential was expected. Following the same logic, the redox behavior of complexes **3**−**5** should be closer to the analogous bis(2-pyridylcarbonyl)amine (bpca) complexes. The $E_{1/2}$ reported for the II → III redox process was −0.28 for cobalt and 0.35 V for iron.[68] These values suggest that the nature of **12** lies somewhere inbetween the bpca and terpy ligands, possibly due to the electron-withdrawing effect of the SCN moieties.
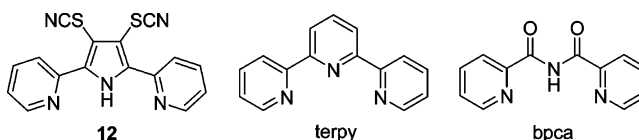

To examine this phenomenon, the redox potential of **4** was compared with that of the SCN-free cobalt compound **10**, which

(62) Behere, D. V.; Mitra, S. *Inorg. Chem.* **1980**, *19*, 992−995.
(63) Chen, W.-Z.; Cotton, F. A.; Dalal, N., S.; Murillo, C. A.; Ramsey, C. M.; Ren, T.; Wang, X. *J. Am. Chem. Soc.* **2005**, *127*, 12691−12696.
(64) Gutlich, P.; Garcia, Y.; Goodwin, H. A. *Chem. Soc. Rev.* **2000**, *29*, 419−427.
(65) Gutlich, P.; Goodwin, H. A. *Top. Curr. Chem.* **2004**, *233*, 1−47.

(66) Rao, J. M.; Hughes, M. C.; Macero, D. J. *Inorg. Chim. Acta* **1976**, *16*, 231−236.
(67) Arana, C.; Yan, S.; Keshavarz-K, M.; Potts, K. T.; Abruna, H. D. *Inorg. Chem.* **1992**, *31*, 3680−3682.
(68) Kajiwara, T.; Sensui, R.; Noguchi, T.; Kamiyama, A.; Ito, T. *Inorg. Chim. Acta* **2002**, *337*, 299−307.
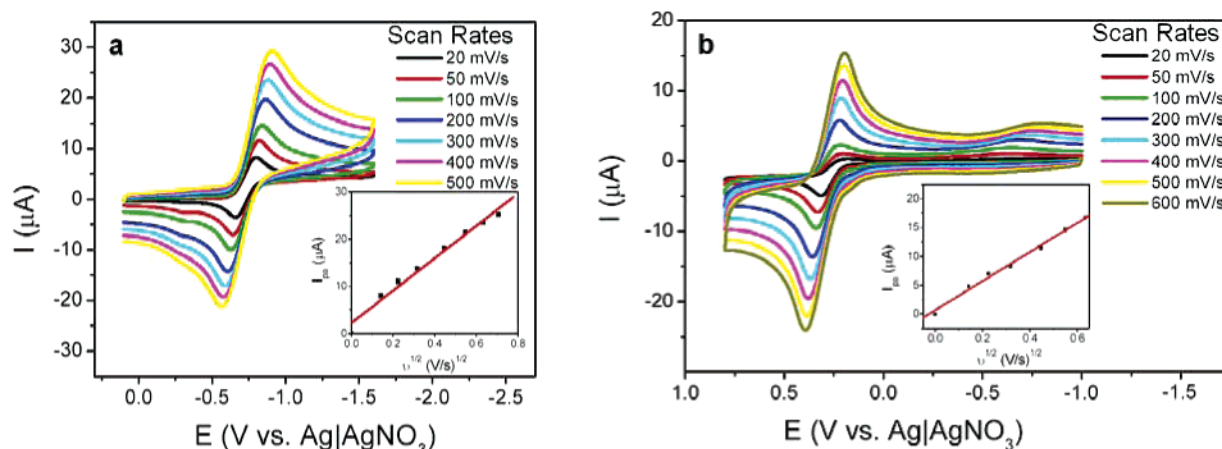
Figure 10. Representative plots of the cyclic voltammetry data. The reversible reduction/oxidation of (a) copper complex **2** and (b) the iron complex **5**. The linear relationship between the oxidation peak currents and square root of scan rates, as shown in the insets, indicates a diffusion-controlled redox process.
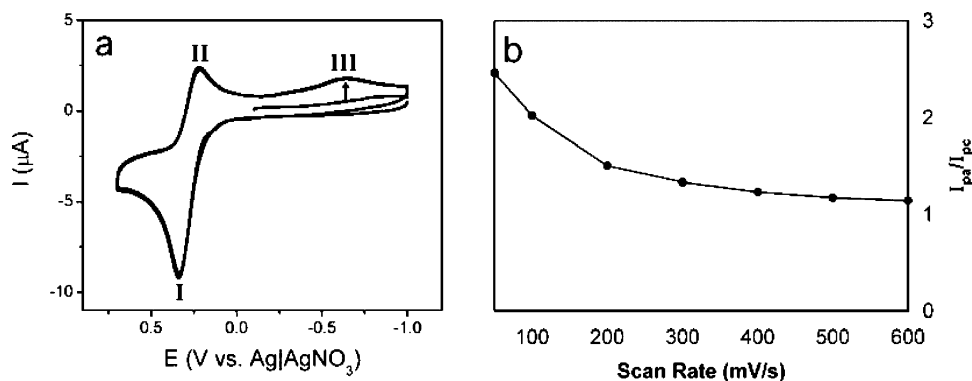
Figure 11. (a) Cyclic voltammagram of **5**. (b) I_{pa}/I_{pc} at various scan rates.
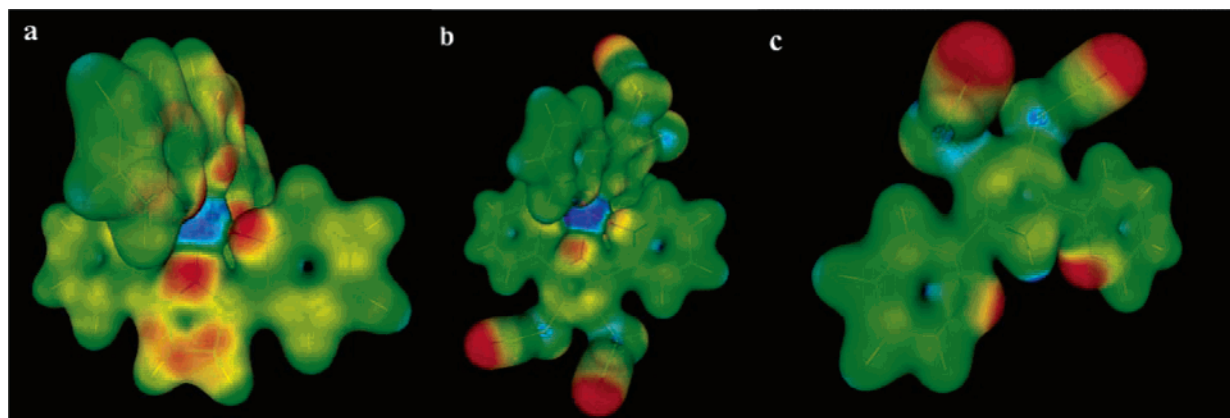
Figure 12. Potential map of **9** (a), **1** (b), and **12** (c). Images are overlaid visualizations of electron density and potential maps. The calculation was performed using the Gaussian 98 software suite[27] with SDD[28,29] basis set on the X-ray crystal structure data. The output was visualized with gopenmol.[30,31] Red denotes the most electron-rich areas, blue, the most electron-deficient.

has its oxidation/reduction at −0.42 and −0.30 V, respectively. From such comparison we see that the thiocyanate moiety has the effect of decreasing the reduction potential of the metal (−0.38 V for **10**, −0.01 V for **4**), apparently by reducing the electron density available in the pyrrole ring, and in turn the metal center. This is further supported by theoretical modeling of the compounds which shows a decrease in the electron density of the pyrrole ring (illustrated in Figure 12) when the thiocyanate moieties are on the pyrrole ring.

Neither the zinc compound **1** or the copper compound **2** are readily oxidized to the metal(III) oxidation state. With the copper compound **2**, the lowest-energy transition is to the metal(I) state.

This reduction and oxidation occurs respectively at −0.80 and −0.66 V. The zinc compound **1**, as expected, shows no oxidation or reduction within a window from +1.0 to −1.6 V.

The zinc compound **1** does, however, show the oxidation and reduction of the thiocyanate group (Figure 13). In agreement with recently published data,[69,70] we clearly see the thiocyanate reduction to thiolate at −2.0 to −2.2 V for **1** (zinc) and **12** and **3** (nickel), and **4** (cobalt) (although in the latter two cases the

(69) Houmam, A.; Hamed, E. M.; Hapiot, P.; Motto, J. M.; Schwan, A. L. *J. Am. Chem. Soc.* **2003**, *125*, 12676−12677.
(70) Houmam, A.; Hamed, E. M.; Still, I. W. J. *J. Am. Chem. Soc.* **2003**, *125*, 7258−7265.
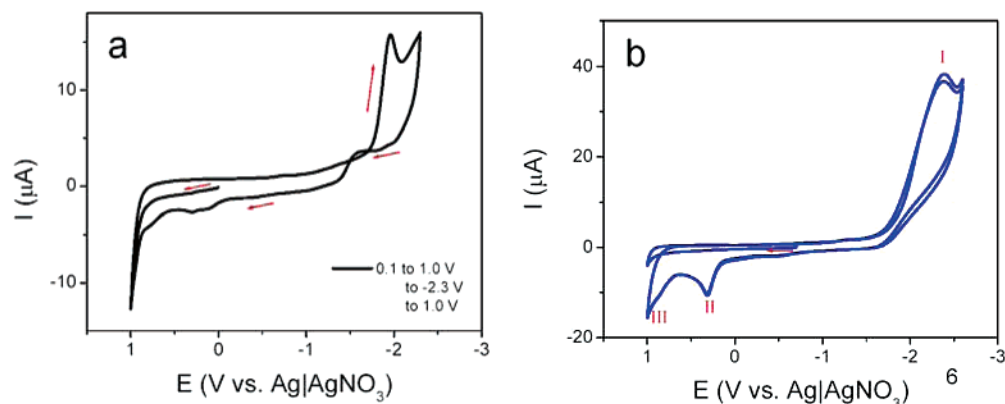
Figure 13. Oxidation and reduction of the SCN moiety. (a) The oxidation and reduction of the free ligand **12**. (b) The oxidation and reduction of **1**.

precise location cannot be determined due to possible metal redox features appearing at nearby potentials). The corresponding oxidation features (ca 0.3 V) are attributed to the formation of disulfide bonds. These data show the sensitivity of the reduction to the electron density in the adjacent ring, as has been demonstrated previously.[69,70] As a general trend, when the ring is electron deficient, the reduction occurs at a more positive voltage. In our experiments the electron-poor ligand **12** shows the reduction at −1.96 V. If these data are then compared to those of the zinc, nickel, and cobalt complexes (−2.2, ∼−2.1, and ∼−2.1 V, respectively), we observe this same trend.

Infrared 4000−400 cm⁻¹ (2500−25000 nm). Several IR assignments can be made unambiguously and can be useful in corroborating the relative electron densities of various parts of the ligand. The most obvious stretch is the $\nu(CN)$ which occurs at ∼2150 cm⁻¹. The signal at ∼680−690 cm⁻¹ can also be attributed to the thiocyanate functionality. The stretches at ∼1590 are $\nu(C=C)$ and $\nu(C=N)$. A stretch at 1583 cm⁻¹ is generally attributed to pyridine C=C and C=N stretches; it is well-known that this stretch shifts to higher wavenumbers for pyridine complexation.[71] In our case the shift is not as large due to the longer than usual pyridine−metal bond length. Most of the other peaks vary too much in location or intensity to make an assignment. The stretches falling between 1520 and 1430 cm⁻¹ belong to the ring breathing ($\nu(C=C)$ and $\nu(C=N)$), with the two stretches at 1460−1430 likely belonging to the pyridine.

These IR assignments can be useful in the discussion of the electronic effects of the metal centers on the SCN reductions. Should the arguments regarding the SCN reduction potentials and their relationships with the electron density of the pyrrole ring (made in the previous section) be valid, we would also expect to see corresponding changes in the SCN frequencies. The trend is obvious in the case of the electron-dependent CN stretch (Table 5). As changes in the electron density of the pyrrole ring for **1−5** are primarily the result of covalent interactions with the metal both of these frequencies should also provide some insight into the amount of delocalization of the ligand electrons onto the metal.

Surface Characterization. Surface characterization of the molecular assemblies focuses on analytically determining which, if any, aspects of the molecule may have changed during the assembly procedure. Although thiocyanates are known to

(71) Gupta, R. R. *Physical Methods in Heterocyclic Chemistry*; Wiley-Interscience: New York, 1984.

Table 5. Thiocyanate Infrared Stretches for the Metal Complexes **1−5** and the Free Ligand **12**

cmpd	12	4	3	5	2	1
metal	None	Co	Ni	Fe	Cu	Zn
SCN reduction	−1.96	∼−2.1	−2.1	-	-	−2.2
$\nu(CN)$, cm⁻¹	2152.0	2150.1	(a)	2149.1	2148.9	2148.7
$\nu(C-S)$, cm⁻¹	733.9	743.8	744.1	743.0	743.7	743.3
$\nu(C-S)$, cm⁻¹	686.6	696.5	699.3	698.3	698.5	699.0

(a) Two separate peaks appear for the nickel compound **3** in the thiocyanate region as a result of a slight difference in bond lengths of one of the thiocyanates.
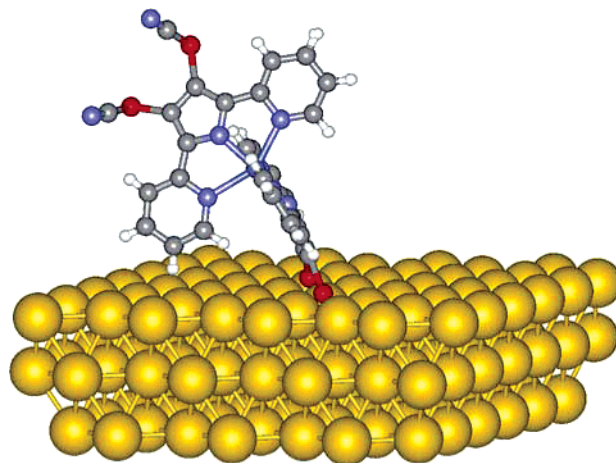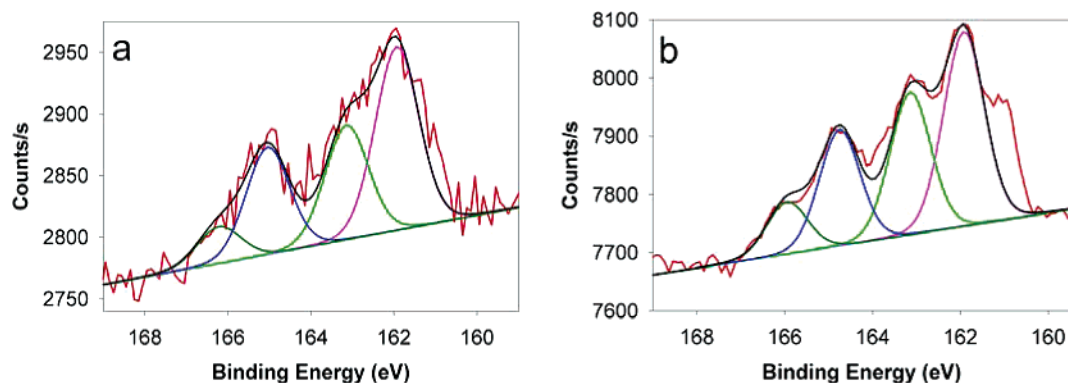

Figure 14. A model of the cobalt-containing molecule **4** assembled on a gold (111) surface.

prevent disulfide polymerization,[22] and the rigidity and orthogonality of the ligands prevent both ligands from binding to gold at the same time (Figure 14), confirmation was needed. We also examined the molecules for ligand loss, metal oxidation/reduction, or ligand decomposition.

X-ray Photoelectron Spectroscopy (XPS). XPS is a powerful tool available for discerning the state of the molecule on the surface. By comparing the spectral data of the powder sample to that of the assembled molecule, we can observe the bonding of the sulfurs, and any change in the oxidation state of the metal center, as well as other changes that may occur upon assembly.

Initially, we sought confirmation that the molecules were covalently bound to the surface. An advantage of the thiocyanate assemblies is that thiolates (Au−S) generated during the assembly have substantially more electron density than the thiocyanates (−SCN) and can be distinguished easily by XPS

Figure 15. Deconvolution of the sulfur 2p region of the XPS spectrum. The left pair of peaks in each figure is due to the thiocyanates (−SCN), the right pair from the thiolates (Au−S). (a) Deconvolution of the S 2p region in the surface-assembled sample of **4**. (b) Deconvolution of the S 2p region in the surface-assembled sample of **2**.

Table 6. Comparison of the XPS Binding Energies of the Powdered and Assembled Forms of **4**

spectral component	surface spectrum binding energy (eV)		powder spectrum binding energy (eV)
S 2p$^{3/2}$	161.9 (Au−S)	165.0 (−SCN)	164.8
S 2p$^{1/2}$	163.2 (Au−S)	166.4 (−SCN)	166.2
Co 2p$^{3/2}$	781.6		780.4
Co 2p$^{1/2}$	796.5		796.3
N 1s	399.3		398.6

(Figure 15a,b).[22,23] Thus, these two peaks are an indication that one set of sulfurs is bound to gold, the other to CN. All compounds showed similar sulfur regions. As a general trend, all thiolate regions were of slightly larger intensity than the thiocyanate region. A possible reason for this discrepancy is that, at several areas on the substrate, surface roughness (which is closer to curvature on the atomic scale) may allow three or four sulfurs to reach the surface. When this is averaged out over all the surfaces, we would expect to see a ratio of thiolate to thiocyanate that is larger than 1:1. However, when assemblies were performed on gold on the flatter mica surface, there was

no change in the S−Au to S−CN ratio from assemblies done on gold−silicon surfaces. Another possibility, disproportionation, is ruled out (vide infra). X-ray meditated decomposition of the thiocyanate can be ruled out as multiple scans in the same region show no difference in intensity. We are left to conclude that the difference is due to a combination of a slight difference in the efficiency of the photoelecton process and/or a charging effect. Charging can retard the formation of photoelectrons. A difference in the effectiveness of the neutralizer on the gold thiolates vs the thiocyanates will in turn cause a difference in the measured intensity by XPS. Since the difference appears consistently from sample to sample, such a mechanism seems likely.

XPS allows the examination of the surface assembly for other signs of change in the molecule. Large changes in binding energy of the elements would be indicative of a change in oxidation state or bonding motif. Table 6 and Figure 16 summarize the binding energies of each element of the complex showing both the powder spectrum and surface assembly. No substantial changes in binding energies were seen, indicating
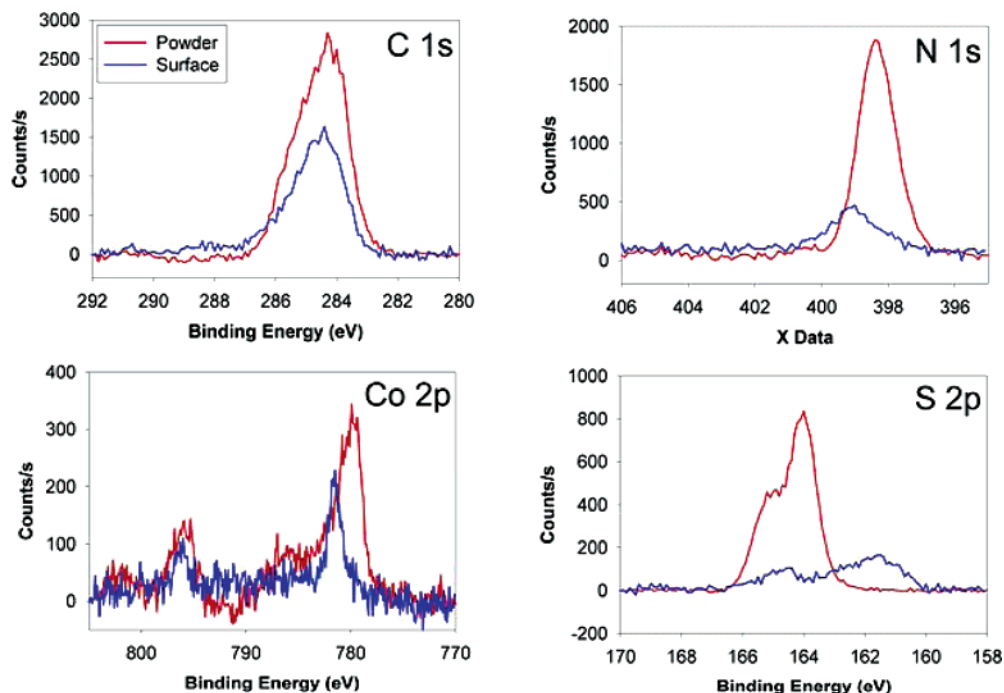
Figure 16. Comparison of powder and surface XPS spectra of **4**. Results are representative of the data for **1**−**4**.

Table 7. Film Thickness ($\pm$10%) for Assemblies[a] of **1**, **3**, **4**

molecule	measured thickness (Å)
Zn (**1**)	13.5
Ni (**3**)	10.5
Co (**4**)	12.8

[a] The calculated height for surface bound-metal complex is 14 Å. The calculated height is the distance from the gold surface to the outermost atom of the complex while taking into account a 20° sulfur tilt angle.

the assembled molecule was similar to the powder form except for the fact that two of the thiocyanates had been converted to thiolates. The small shift in both nitrogen and cobalt energies can be attributed to the difference in electron density of the ligand when the electron-withdrawing thiocyanates are converted to electron-rich thiolates. According to atomic concentration calculations performed using the PHI Multipak software, the ratio (corrected for the atomic sensitivity factors of each respective element) of cobalt to S in the crystalline powder sample of **4** matched the ratio found in the surface-assembled sample. This indicates that the metal complex has not disproportionated or decayed and is most likely intact on the surface.

Ellipsometry. Ellipsometry was carried out on the self-assembled monolayers (SAMs). Due to the bulky nature of the molecules we did not expect the packing to approach the theoretical height of the molecule. For a layer of bulky molecules on the surface we would expect a thickness of about 11−12 Å,[72] while for a well-packed monolayer the thickness would be 14 Å. Ellipsometric values lie between these two, but do not give a definitive indication due to the error in the measurement. Thiocyanate assembly has been previously shown to prevent multilayers,[22] and ellipsometry confirms this for these complexes (Table 7).

Infrared Reflection Spectroscopy Measurements. IR reflection spectroscopy was used for a secondary confirmation of the presence of the thiocyanate after assembly. Both the nickel and cobalt complexes were examined. In both cases the

(72) Wu, C.-G.; Chiang, S.-C.; Wu, C.-H. *Langmuir* **2002**, *18*, 7473−7481.

Table 8. Stretching Frequencies of the CN Triple Bond

cmpd	ν(CN) (powder) cm^{-1}	ν(CN) (surface) cm^{-1}
3	2155.6, 2146.8	2156.5, 2147.1
4	2150.1	2151.7

thiocyanate was clearly visibly by IR and had a stretch nearly identical to that of the powder. The surface stretch had shifted ~1 cm^{-1} higher but appeared at values similar to those of the powder spectrum (Table 8).

Conclusions

We have shown a simple and efficient method for the synthesis of the transition metal complexes **1**−**5**. Characterization of these compounds via UV−vis, cyclic voltammetry, magnetic susceptibility, and EPR allows us to predict and explain many of the electronic properties of these molecules in SMTs. The complexes have a high degree of covalency between the metal core and ligands, explaining the origin of high Kondo temperatures in SMTs. Assembly of the molecules on gold gives a thickness consistent with what is expected for a loosely packed layer of bulky molecules. Other surface characterizations (XPS, surface IR) show species pre- and post- assembly that are virtually identical except for the two thiocyanates that have been converted to thiolates during assembly.

Supporting Information Available: Synthetic details, characterization data, and the complete ref 28. This material is available free of charge via the Internet at http://pubs.acs.org.

JA055459D